

# Chapter 1

## Theory

In this chapter we review and develop the theory required to model signal transmission from cosmic source to uncalibrated (raw) interferometric data. The first half of this chapter provides the necessary introduction to fundamental radio interferometric concepts while the second half is focused specifically on describing several key signal corruptions, relevant to mm-VLBI observations.

### 1.1 Radio Interferometry

This section is structured as follows: first radio interferometry is introduced using the Radio Interferometric Measurement Equation (RIME) formalism, which serves as a guiding framework for the construction of the MEQSIL-HOUEETTE simulator. We then review the technique of self-calibration, typical mm-VLBI data products and the consequences of breaking the static source assumption.

### 1.1.1 Measurement Equation

The RIME provides the notation and formalism to model the signal transmission path as a sequence of linear operations. It takes into account polarisation, correlation and the correct time-ordering of signal transmission path in an intuitive and efficient way. The formalism also enables a more informative phrasing of the relation between calibration and signal corruptions.

Here we offer a short derivation and explanation of the RIME following Smirnov [2011a]. Consider a quasi-monochromatic, complex-valued electric field vector  $\mathbf{E}$ , which can be decomposed into an arbitrary two dimensional orthogonal basis in the plane perpendicular to the direction of propagation,

$$\mathbf{E} = \begin{pmatrix} E_a \\ E_b \end{pmatrix},$$

where this choice represents the basis in which the polarisation is measured. All linear transformations of the above electric field can be written by a multiplication with a 2 x 2 complex valued matrix, termed a *Jones* matrix [?][ads was down!],

$$\mathbf{E}' = \mathbf{J}\mathbf{E}. \quad (1.1)$$

For example, the conversion of the electric field to a voltage  $\mathbf{v}$  at an antenna can be specified by such a transformation i.e.  $\mathbf{v} \equiv \mathbf{E}'$  under multiplication with the appropriate  $\mathbf{J}$ . Multiple effects then can be represented by multiplication of various Jones matrices, forming a Jones chain,

$$\mathbf{E}' = \mathbf{J}_n \dots \mathbf{J}_1 \mathbf{E}. \quad (1.2)$$

The order of the Jones matrices should obey the casual order of the signal transmission path (i.e.  $\mathbf{J}_1$  would be closest to source,  $\mathbf{J}_n$  closest to antenna). However the rules of commutativity of matrices allows us some flexibility. Matrices which are scalar commute with everything, while diagonal matrices commute with each other as do matrices which effect a rotation of  $\mathbf{E}$ . This

allows the Jones chain to be re-ordered into more convenient formulations as required. In other words, the signal path can be parameterised in different ways. For example during calibration, it is useful to construct a *phenomenological* Jones matrix which represents the combined action of several *physical* commuting processes/matrices (e.g. ionospheric delay and electronic drift). The advantage would be that only the cumulative effect is considered, which keeps the number of parameters to solve for to a minimum. This would be useful when the individual effects cannot be easily distinguished and/or have the same Jones matrix form. On the other hand, for realistic data simulation, we prefer to model the signal transmission path by formulating a Jones matrix based on the exact physical process.

An interferometer measures the correlation of the voltages from an antenna pair, referred to as a *baseline*. The correlator output is termed the *visibility*,

$$\mathbf{V}_{pq} = \langle \mathbf{v}_p \mathbf{v}_q^H \rangle, \quad (1.3)$$

where  $p, q$  refer to the two antennae. The representation of  $\mathbf{V}_{pq}$  as a  $2 \times 2$  matrix is equivalent to the Stokes polarisation formulation, for example in an XY basis,

$$\mathbf{V}_{pq} = \mathbf{J}_p \langle \mathbf{E}_p \mathbf{E}_q^H \rangle \mathbf{J}_q^H \quad (1.4)$$

$$= \mathbf{J}_p \begin{pmatrix} \langle E_{xp} E_{xq}^* \rangle & \langle E_{xp} E_{yq}^* \rangle \\ \langle E_{yp} E_{xq}^* \rangle & \langle E_{yp} E_{yq}^* \rangle \end{pmatrix} \mathbf{J}_q^H \quad (1.5)$$

$$= \mathbf{J}_p \begin{pmatrix} I + Q & U + iV \\ U - iV & I - Q \end{pmatrix} \mathbf{J}_q^H, \quad (1.6)$$

where  $I$  is the coherence of the total flux,  $V$  is the coherence of the circularly polarised flux,  $Q$  and  $U$  relate to coherence of the linear polarisation. Note that the Jones matrices are assumed to be constant over the time and frequency averaging interval. As this formalism is coordinate system inde-

pendent, we can easily transform any  $2 \times 2$  from a linear to circular basis and vice-versa.

We now review the RIME for a single, uncorrupted, unpolarised point source, which will illustrate the Fourier transform relation between the measured visibility and a section of approximately flat sky. Considering that there are no signal corruptions, the only Jones matrix to consider is the effect of the phase difference of the electric fields measured at the two antennae. This is due to the difference in propagation path length.

Consider the vector  $\boldsymbol{\sigma}$  which points from the centre of the Earth towards the source. We define the position difference between the two antenna or baseline vector  $\mathbf{u} = (u, v, w)$  with the  $w$ -axis in the direction of  $\hat{\boldsymbol{\sigma}}$ . Next we denote the angular position on the sky by  $(l, m)$  which are the directional cosines on the sky measured in the direction of  $(u, v)$  respectively. Note that we consider only a small approximately flat section of the celestial sphere centred on  $\boldsymbol{\sigma}$ , also called the *phase centre*. The phase difference between rays arriving at the two antenna is therefore,

$$\delta\phi = 2\pi(\mathbf{u}/\lambda \cdot \boldsymbol{\sigma}) \quad (1.7)$$

As we are only interested in a small approximately planar component of the sky (i.e.  $l^2 + m^2 \ll 1$ ),

$$\delta\phi = 2\pi\lambda^{-1}(u_pl + v_pm). \quad (1.8)$$

Denoting the brightness matrix  $\mathbf{B} = \langle \mathbf{E}_p \mathbf{E}_q^H \rangle$  and setting the delay of antenna  $q$  as the reference, the RIME for our simplified model becomes

$$\mathbf{V}_{pq} = \mathbf{K}_p \mathbf{B} \mathbf{K}_q^H \quad (1.9)$$

$$= \exp(2\pi i \lambda^{-1}(ul + vm)) \mathbf{B}(1) \quad (1.10)$$

where  $\mathbf{K}$  was the Jones matrix used to apply the phase difference to each

antenna. This is a Fourier Transform relation between visibility domain  $(u, v)$  and image domain  $(l, m)$ . This derivation can be easily extended to sources (e.g. see [Smirnov, 2011a]). The quantity  $K_p \mathbf{B} K_q^H$  is often denoted as  $\mathbf{X}_{pq}$  and is termed the coherency matrix.

An example of a Jones matrix representing a signal corruption is the complex time-variable antenna gain. Considering two independent linear dipoles, for antenna p

$$\mathbf{G}_p(t) = \begin{pmatrix} g_x(t) & 0 \\ 0 & g_y(t) \end{pmatrix} \quad (1.11)$$

Hence the RIME in this case becomes,

$$\mathbf{V}_{pq} = \mathbf{G}_p \mathbf{X}_{pq} \mathbf{G}_q^H \quad (1.12)$$

### 1.1.2 A primer on self-calibration

Self-calibration, as the name suggests, uses the target itself as a calibrator to estimate station gains. In mm-VLBI calibration, self-calibration is applied under two different formulations. The first is a procedure termed *fringe fitting*. From the point of view of the RIME, fringe-fitting solves for station gains in equation ?? over a time interval typically on the order of minutes. Taking a linear expansion in frequency and time of the phase of the station gain yields,

$$\begin{aligned} \mathbf{V}_{pq}(t_0, dt, \nu_0, d\nu) &= |G_p| |G_q| \mathbf{X}_{pq} \exp(i[\phi_p(t_0, \nu_0) + \partial_t \phi_p(t, \nu_0) dt \\ &\quad + \partial_\nu \phi_p(t_0, \nu) d\nu - \phi_q(t_0, \nu_0) - \\ &\quad \partial_q \phi_p(t, \nu_0) dt - \partial_\nu \phi_q(t_0, \nu) d\nu]). \end{aligned} \quad (1.13)$$

A blind search is then performed for all the station based parameters in the above equation i.e. everything except  $\mathbf{X}_{pq}$ . The station gain amplitude

will sometimes be calibrated separately, reducing the number of parameters to solve. The sky model used is typically just a point source at the centre of the field.

The second formulation of self-calibration (which I will just refer to as self-calibration) is to iteratively solve for station gains but not their derivatives whilst constructing the sky model. We begin with the initial sky model (typically a point source) as well as the station gains output by the fringe fit. Then we solve equation ?? using a least squares procedure but without taking into account station gain phase derivatives so that there are fewer free parameters. The resulting dataset is then imaged, deconvolved (i.e. the effect of the synthesised beam is removed) and a source finder is applied on the image to construct a more accurate sky model. This sequence is then repeated with the updated sky model being used when solving for station gains. The loop will terminate when a specified flux threshold is reached.

The interaction of both fringe fitting and self-calibration with a variable source, tropospheric, ISM and instrumental signal corruptions is of central interest to this investigation.

### 1.1.3 mm-VLBI observables and data products

If the visibility phase is highly variable as in the case of a turbulent atmosphere, conventional calibration and imaging techniques have severely limited (if any) success. However information can still be extracted from the raw visibilities in the form of closure quantities [?] or polarisation ratios [?]. Visibility amplitudes are also used although they suffer from systematic errors, a subset of which are dealt with in this work. There also exist imaging algorithms [e.g. Lu et al., 2014, Bouman et al., 2015, Chael et al., 2016] which use closure phase as a regulariser to ensure that miscalibration of station gains do not effect the resulting image, although these unconventional imaging algorithms come with their own uncertainties on fidelity. Closure phase, defined as the sum of 3 visibility phases of a triangle of stations  $\{i, j, k\}$ , is

a probe of point-asymmetry in source structure,

$$\Phi_{ijk} = \phi_{ij} + \phi_{jk} + \phi_{ki}. \quad (1.14)$$

Because most signal corruptions are station based, the gain phase terms  $\phi_{ij} = \phi^{\text{true}} + \phi_i^G - \phi_j^G$  for each antenna, assuming constant over the integration time and bandwidth will cancel, yielding a more robust observable.

In the literature, the uncertainty on the closure phase is calculated in various ways. One method is model dependent [?] and is given as a function of the SNR  $s$  of each baseline

$$u(\Phi_{ijk}) = \frac{\sqrt{4 + (s_{ij}s_{jk})^2 + (s_{jk}s_{ki})^2 + (s_{ij}s_{ki})^2 + 2(s_{ij}^2 + s_{jk}^2 + s_{ki}^2)}}{s_{ij}s_{jk}s_{ki}}, \quad (1.15)$$

where  $s_{ij}$  is defined as

$$s_{ij} = |V_{ij}| \sqrt{\frac{\tau \Delta \nu}{SEFD_i SEFD_j}}, \quad (1.16)$$

where  $\tau$  is the vector averaging timescale,  $\Delta \nu$  is the bandwidth,  $|V_{ij}|$  is the visibility amplitude and  $SEFD$  is the system equivalent flux density.

Alternatively, assuming Gaussian errors the uncertainty on the closure phase over a scan  $u(\Phi_{ijk}) = \sigma(\Phi_{ijk})/\sqrt{(n)}$  [?].

#### 1.1.4 Variability and the static source assumption

Implicit in our description of interferometry above (e.g. equation ??), we assumed that the source remains approximately unchanged or static during the course of the observation. However, if this assumption does not hold (i.e. if the source is time-variable), the visibilities measured over the course of an observation can no longer be related to a single image. Note that I am using

the term ‘variability’ in a general sense which refers to changes in any source observables. ‘Variability’ is most often used to denote changes in source flux but we extend the definition to include changes in source structure, position and polarisation. We expect that an image of a variable source would appear smeared out as it is averaged over many realisations and that ghosts should arise during the calibration/deconvolution procedure [citations? trienko’s papers?]. One of the objectives of this thesis will be to characterise the errors which emerge when a variable source is self-calibrated in the presence of tropospheric-induced errors. Practically it is difficult to separate source and instrumental variability without accurate models for both.

Although the static source assumption holds for most interferometric observations, the accretion flow and/or magnetic field structures around a SMBH can be variable on far shorter timescales. The primary mm-VLBI target, Sgr A\*, exhibits variability on timescales of minutes to hours in the radio (including EHT observations), near-infrared (NIR), and X-ray bands [e.g. ??????]. This wealth of observational data has yielded several answers but the origin of the variability is still highly debated. To explain the observed delays between flares in different frequency bands, an expanding adiabatic plasma model (Marrone, 2008) has been presented however a recent flare observed with the EHT did not exhibit the increase in size expected from an expanding plasma outflow model ?. Signatures of periodic variability at NIR and x-ray [?] have been used to argue for the presence of orbiting hotspots Doeleman et al. [2009]. As the Innermost Stable Circular Orbit (ISCO) depends on spin of the BH, the spin can be constrained through the detection periodic orbital features. On the other hand, a more recent observation of a longer light curve in the NIR is more representative of a power-law scale variability ?. The cumulative evidence of these observations point to the possibility of multiple flaring mechanisms. An important mm-VLBI observational result is that variability in the polarisation domain is far more rapid than the total intensity (Johnson 2015b), indicating that



the magnetic fields structure is highly dynamic.

In principle, the variability timescale could be comparable to the period of the Innermost Stable Circular Orbit (ISCO), which for Sgr A\*, ranges from 4 minutes in the case of a maximally rotating BH with a prograde disc to about half an hour for a non-rotating BH. The ISCO period for M87 is substantially longer, on the order of days [refs]. Considering light crossing times  $\Delta t_{\text{cross}}$ , we can estimate the angular size  $\theta$  of the emission region to be of order  $\theta \sim \Delta t_{\text{cross}} c / D_{\text{src}}$ , where  $c$  is the speed of light and  $D_{\text{src}}$  is the observer-source distance. Hence for Sgr A\* at  $D_{\text{src}} = 8.3$  kpc (Gillessen, 2009), a flare of duration  $\Delta t_{\text{cross}} = 10$  min corresponds to scales of  $15 R_{\text{Sch}}$ . Such analyses gave early evidence for an emission area on event horizon scales.

In the case of a highly localised flare, several approaches [Doeleman et al., 2009, ?, ?] show that EHT can track such a structure with  $\sim 5 \mu\text{-arcsec}$  precision using closure quantities and polarimetric ratios. This could help map the spacetime around the BH. Alternatively Lu et al. [2016] show that a gaussian weighting scheme can be applied to mitigate the effects of variability and measure the quiescent structure although this approach would downweight the longest baselines. However all of these approaches assume only gaussian thermal noise, gaussian-blurring in the ISM and no tropospheric-induced calibration errors.

## 1.2 Signal Corruptions

We begin with an introduction to scattering theory, which is applicable to the radiative processes occurring in both the troposphere and ISM. Following this we explore signal corruptions due to the transmission through the ISM and Earth’s atmosphere as well as instrumental imperfections in detail.

### 1.2.1 Scattering basics

Millimetre wavelength radiation originating at the Galactic Centre is repeatedly scattered along the signal path to the Earth-based observer. The first occurrence is due to electron plasma in the ISM [e.g. ??], while the second is due to poorly-mixed water vapour in the Earth's troposphere [e.g. ??]. It is essential that the effects of the scattering phenomena are understood for accurate calibration and robust inference of the intrinsic source properties. To this end, simulation modules approximating scattering in both media are implemented in MEQSILHOUETTE. As an introduction to the separate descriptions of each, we review a simple scattering model.

An electro-magnetic wave is scattered when it passes through a medium with refractive index inhomogeneities. Following ?, this effect can be modeled as a thin screen, located between source and observer planes and orientated perpendicular to the line-of-sight. The screen, indexed by coordinate vector  $\mathbf{x}$ , adds a stochastic phase  $\phi(\mathbf{x})$  to the incoming wave at each point on the screen, yielding a corrugated, outgoing wavefront. We define the Fresnel scale as  $r_F = \sqrt{\lambda D_{os}/2\pi}$ , where  $D_{os}$  is the observer-scatterer distance, or the distance where the geometrical path difference  $\frac{2\pi}{\lambda}(D_{os} - \sqrt{D_{os}^2 + r_F^2}) = \frac{1}{2}$  rad.

To determine the resultant electric field at a point in the plane of the observer, indexed by coordinate vector  $\mathbf{X}$ , one has to take into account all possible ray paths from the screen to  $\mathbf{X}$ . To illustrate the model, a calculation of the scalar electric field generated by a point source,  $\psi(\mathbf{X})$  yields the Fresnel-Kirchoff integral [?]

$$\psi(\mathbf{X}) = C \int_{\text{screen}} \exp \left[ i\phi(\mathbf{x}) + i\frac{(\mathbf{x} - \mathbf{X})^2}{2r_F} \right] d\mathbf{x}, \quad (1.17)$$

where  $C$  is a numerical constant.

The statistical properties of  $\phi(\mathbf{x})$  can be described by a power spectrum

or equivalently the phase structure function,

$$D_\phi(\mathbf{x}, \mathbf{x}') = \langle [\phi(\mathbf{x} + \mathbf{x}') - \phi(\mathbf{x})]^2 \rangle, \quad (1.18)$$

where  $\mathbf{x}$  and  $\mathbf{x}'$  represent two points on the screen and  $\langle \dots \rangle$  denotes the ensemble average.

There is evidence that  $D_\phi$  can be reasonably approximated by a power law dependence on the absolute distance  $r$  between points on the screen [??]

$$D_\phi(r) = (r/r_0)^\beta, \quad r^2 = (\mathbf{x} - \mathbf{x}')^2 \quad (1.19)$$

where  $r_0$  is the phase coherence length scale defined such that  $D_\phi(r_0) = 1$  rad. Kolmogorov turbulence, which describes how kinetic energy injected at an outer length scale  $r_{\text{out}}$  cascades to increasingly smaller scales until finally dissipated at an inner length scale  $r_{\text{in}}$ , predicts  $\beta = 5/3$  in the domain  $r_{\text{in}} \ll r \ll r_{\text{out}}$ . This scaling has been demonstrated to be a reasonable approximation for the ISM over scales  $r \sim 10^2$  km to  $> 1$  AU [?], and also for the troposphere with  $r < \Delta h$ , where  $\Delta h$  is the thickness of the turbulent layer ?. The specifics of the tropospheric model will be explored further in later sections.

The two length scales,  $r_F$  and  $r_0$ , define the nature of the scattering which is split into the strong and weak regimes, Fig. ???. In weak scattering,  $r_0 \gg r_F$  and hence by equation ??,  $D_\phi(r_F) \ll 1$ . This implies that most of the radiative power measured on a point  $\mathbf{X}$  will originate from a screen area  $A_{\text{weak}} \approx \pi r_F^2$ . Whereas in the regime of *strong scattering*,  $r_0 \ll r_F$  yielding  $D_\phi(r_F) \gg 1$ . This results in coherent signal propagation onto the point  $\mathbf{X}$  from multiple disconnected zones each of area  $A_{\text{strong}} \approx \pi r_0^2$  [?]. Scattering in the troposphere and ISM in the direction of the Galactic Centre fall into the regimes of weak and strong scattering respectively.

To evolve the screen in time, we assume a frozen screen i.e. that the velocity of the individual turbulent eddies is dominated by the bulk motion

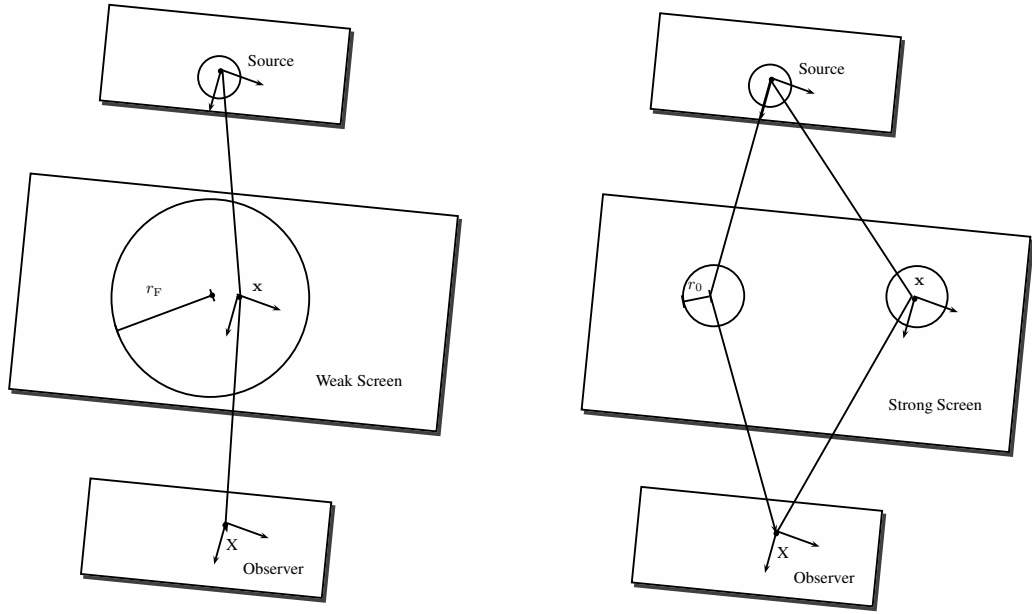


Figure 1.1: Illustration depicting the basics of scattering in the weak (left) and strong (right) regimes. In the weak regime, the signal is coherently propagated over an area,  $A_{\text{weak}} \approx \pi r_F^2$ , whereas in the strong regime, coherent propagation is split over many areas, each of size  $A_{\text{strong}} \approx \pi r_0^2$ .

of scattering medium [e.g. ?]. This allows us to treat the screen as frozen but advected over the observer by a constant motion. Hence time variability can be easily incorporated by the relative motion between source, scattering screen and observer.

### 1.2.2 Interstellar medium scattering

Electron density inhomogeneities in the interstellar medium (ISM) plasma scatter the radio emission from the Galactic Centre. Radio interferometric observations of Sgr A\* have characterised the basic properties of the intervening plasma material, however extensive developments in scattering theory and simulations have proved essential to the interpretation of more subtle scattering phenomena. This section begins with the earlier, longer wavelength VLBI results which studied the Gaussian blurring effect of the scattering of SgrA\*; we then expand on the scattering theory introduced in Sec. ?? to review the latest theoretical developments which explore the presence of scattering-induced substructure; finally we review recent observational results which account for scattering substructure in their data interpretation.

The dominant observational effect of this scattering scenario for  $\lambda \gtrsim 1$  cm is to convolve the intrinsic source structure with an elliptical Gaussian. The size of the Gaussian exhibits a  $\lambda^2$  scaling dependence over several orders of magnitude [Fig. ?? ????], which is consistent with the wavelength dependence of the refractive index of a plasma. In order to determine the parameters of the scattering kernel, i.e. major axis, minor axis and position angle, one has to observe at wavelengths where the angular size of scattering ellipse is much larger than the expected source size. A Very Long Baseline Array (VLBA) + Green Bank Telescope (GBT) campaign ? estimated the size at  $1.31 \times 0.64$  mas  $\text{cm}^{-2}$ , oriented  $78^\circ$  east of north.

An accurate extrapolation of scattering kernel to 1.3 mm is important for the EHT scattering-mitigation strategy Fish et al. [2014] which aims to deblur the scattered image through a deconvolution procedure. However as this

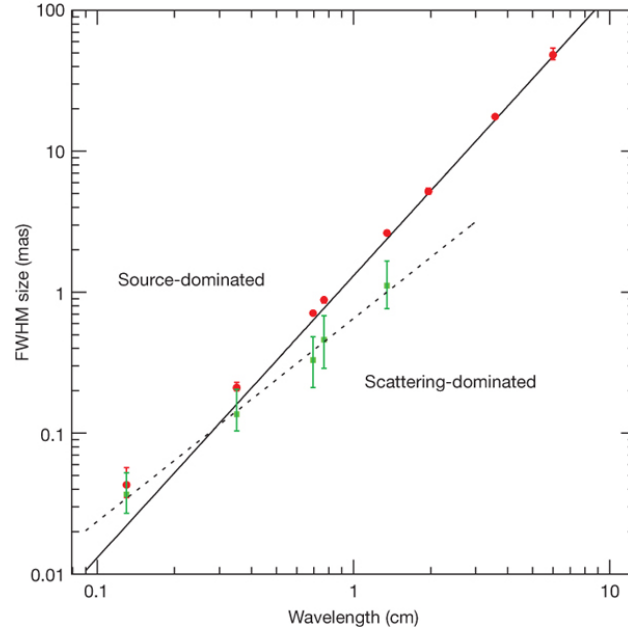


Figure 1.2: The  $\lambda^2$  dependence of scattering kernel size is shown by the solid line. This has been derived from measurements made at  $\lambda > 17$  cm ?. The dotted line shows the derived intrinsic source size which scales as  $\lambda^{1.44}$ . This was derived from measurements in the wavelength range,  $2 \text{ cm} < \lambda < 1.3 \text{ mm}$  [Doeleman et al., 2008]. The red circles show major-axis observed sizes of Sgr A\* and the green points show the derived intrinsic major-axis size. This plot was reproduced from Doeleman et al. [2008].

extrapolation is over at least an order of magnitude, any small systematic error in the original measurement can significantly effect the 1.3 mm extrapolated parameters. A recent review of VLBI observations of Sgr A\* ? has noted that there are significant inconsistencies between different measurements. The authors used a Bayesian methodology to re-analyse the datasets resulting in increased uncertainties as shown in table ???. The minor axis has a much larger uncertainty than the major axis due to the limited north-south coverage of the VLBA array.

The Gaussian blurring effect can explained by the simple scattering model

Table 1.1: A re-analysis of VLBI observations of Sgr A\* by ? has yielded revised estimates of the parameters associated with the Gaussian scattering kernel. Note that the position angle is measured East of North.

major axis FWHM (mas/cm <sup>-2</sup> )	1.32	0.04
minor axis FWHM (mas/cm <sup>-2</sup> )	0.82	0.21
position angle (°)	77.8	9.7

introduced in Sec. ???. Recall, that in the strong scattering regime light is propagated from coherent patches with linear size  $\sim r_0$ . Each patch will emit light coherently into a single-slit diffraction cone of angular size  $\theta_{\text{scatt}} \sim \lambda/r_0$ . An observer will hence be illuminated by many patches spanning  $\theta_{\text{scatt}}$ , yielding a blurred and broadened image, with projected size on the screen equal to the *refractive scale*

$$r_{\text{ref}} = \theta_{\text{scatt}} D_{\text{os}} = r_{\text{F}}^2/r_0.$$

$r_{\text{ref}}$  is the third fundamental length scale in the strong scattering regime and is associated with the refractive timescale,

$$t_{\text{ref}} = r_{\text{ref}}/v.$$

We can calculate  $r_0$  given the FWHM of  $\theta_{\text{scatt}}$  through the more precise relation

$$\theta_{\text{scatt}} = \frac{2\sqrt{2\ln 2}}{2\pi} \lambda/r_0 (M+1) \quad (1.20)$$

where  $M = D_{\text{os}}/R$  is the magnification and  $R$  is the source-screen distance. The magnification factor is a correction to the model introduced in Sec. ?? when  $R \approx \infty$  no longer holds and should be used when calculating distances in the observer plane [?]. The location of the scattering medium was originally thought to be quite close to Sgr A\*. However, observations of a newly discovered pulsar, SGR J1745-29, indicate that the scattering screen is located at a distance  $D_{\text{os}} = 5.8 \pm 0.3$  kpc, within the Scutum spiral arm. Using

Eq. ?? and the parameters given in table ??, we find that the major axis of the coherence length at 1.3 mm,  $r_0 \approx 3136.67$  km.

As the VLBI moves to higher frequencies, focus has shifted away from the well-studied Gaussian convolution effect of ISM scattering and onto the presence of stochastic scattering-induced substructure. To understand this phenomenon, we must first develop the theory to be sensitivity to the averaging effects of the observation.

Strong scattering can be further subdivided into *snapshot*, *average* and *ensemble-average* regimes [??]. To understand the different regimes, remember that for each point on the source, the observer sees emission from coherent patches of area  $\sim \pi r_0^2$  over an area  $\sim \pi r_{\text{ref}}^2$ . The diffraction cones from each of the patches will interfere, resulting in a multi-slit *diffractive scintillation* pattern.

In the *snapshot regime*, a compact source is observed with a narrow bandwidth and over a short time integration. This yields a single realisation of the diffractive scintillation pattern. By averaging over many snapshots, diffractive scintillation is quenched. This occurs if the source size  $\theta_{\text{src}}$  is much larger than the diffractive scale  $\theta_{\text{src}} \gg r_0/D_{\text{os}}$ ; if the fractional bandwidth  $\delta\nu/\nu$  is much larger than the decorrelation bandwidth  $\delta\nu/\nu \gg \delta\nu_{\text{dc}}/\nu \approx (r_0/r_{\text{F}})^2$  [?]; or if the integration time  $t_{\text{int}}$  is much larger the diffractive timescale  $t_{\text{int}} \gg t_0 = r_0/v$ , where  $v$  is the relative velocity between screen, source and observer. This regime is hence only accessible through observations of compact objects like pulsars. On a side note, observations in this regime can be used to probe the source with angular resolution  $\sim \lambda/r_{\text{ref}}$  [e.g. ?]. This is because the scattering screen is essentially a lens of diameter  $\approx r_{\text{ref}}$ .

In the *average regime*, diffractive scintillation has been averaged over, however there still exists scintillation over scales comparable to the size of the scattered image of a point source  $\sim r_{\text{ref}}$ , termed *refractive scintillation*. Phase fluctuations on this scale acts like a weak lens to focus or defocus the  $\lambda/r_0$  scale diffraction cones in the direction of the observer. For a point source



this would lead to weak flux variations in the total flux [?]. We will show later that refractive scintillation leads to the presence of substructure for a resolved scatter-broadened source. In contrast to diffractive scintillation, refractive scintillation is much more difficult to average over. Typically the refractive time scale  $t_{\text{ref}} = r_{\text{ref}}/v$  is on the order of weeks to months for scattering towards the Galactic Centre; the fractional decorrelation bandwidth is on the order of unity  $\delta\nu_{\text{dc}}/\nu \sim 1$ ; and the source has to be much larger than the image of a scattered point source  $\theta_{\text{src}} \gg \theta_{\text{scatt}}$ .

In the *ensemble-average regime*, both diffractive and refractive scintillation have been averaged over. It is in this regime when the scattering is equivalent to Gaussian convolution which is deterministic and not time variable.

A recent theoretical work [?] has derived a useful approximation of the resolved scattered image  $I_{\text{ss}}$  in the average regime,

$$I_{\text{ss}}(\mathbf{x}) \approx I_{\text{src}}(\mathbf{x} + r_{\text{F}}^2 \nabla \phi(\mathbf{x})), \quad (1.21)$$

where  $\nabla$  is the directional derivative. Here we have used the same two-dimensional coordinate system, indexed by  $\mathbf{x}$  to describe the source, screen and observer planes which are considered to be aligned along the vertical axis. The scattered image  $I_{\text{ss}}$  is approximated by a ‘reshuffling’ of the source image  $I_{\text{src}}$ . As  $|\nabla \phi| \sim 1/r_0$ , the magnitude of the translation of points on  $I_{\text{src}} \sim r_{\text{ref}} \sim 10 \mu\text{-arcsec}$  in the case of Sgr A\*.

Even though  $\phi(\mathbf{x})$  is only coherent to  $\sim r_0$ ,  $\nabla \phi(\mathbf{x})$  remains spatially coherent over much larger scales. The autocovariance of phase derivative can be related to the structure function [?]

$$\langle [\partial_x \phi(\mathbf{x}_0)] [\partial_x \phi(\mathbf{x}_0 + \mathbf{x})] \rangle = \partial_x^2 D_\phi(\mathbf{x}). \quad (1.22)$$

A generalised structure function [??] is quadratic ( $r^2$ ) at small scales ( $r \ll r_{\text{in}}$ ), Kolmogorov in the range  $r_{\text{in}} < r < r_{\text{out}}$  and constant for  $r > r_{\text{out}}$ .

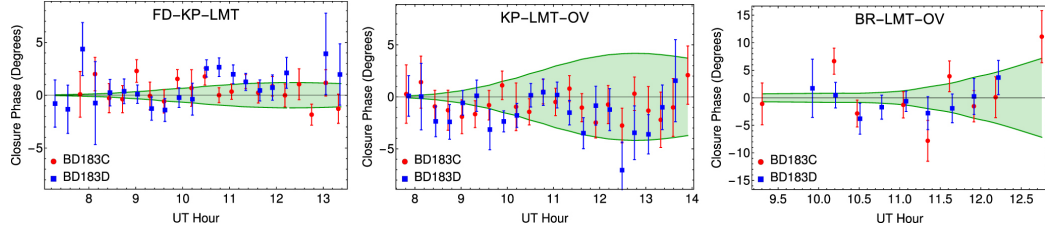


Figure 1.3: Closure phases recorded in a VLBA + LMT observation of Sgr A<sup>\*</sup> at  $\lambda = 3.5$  mm. The data points are shown as red circles and blue squares and are only distinguished by the calibrator used. The green envelopes show the  $1\sigma$  closure phase prediction induced by scattering-induced substructure. Reproduced from [?].

Taking the simplifying case of  $r_{\text{in}} \gg r_0$  and  $r_{\text{in}} < r < r_{\text{out}}$   $D_\phi$  becomes[?],

$$D_\phi = \frac{2}{\beta} \left( \frac{r_{\text{in}}}{r_0} \right)^{2-\beta} \left( \frac{r}{r_0} \right)^\beta \quad (1.23)$$

Hence,  $\partial_r^2 D_\phi(\mathbf{r}) \propto r^{\beta-2}$ . Therefore in the Kolmogorov regime ( $\beta = 5/3$ ), the coherence of image shift relative to the refractive scale  $\propto (r/r_0)^{-1/3}$ . Note that a large inner scale extends coherence of  $\nabla\phi$ , whereas as  $r \rightarrow r_{\text{out}}$  the coherence falls quickly. Therefore, even though  $\phi(\mathbf{x})$  is only coherent to  $\sim r_0$ ,  $\nabla\phi(\mathbf{x})$  remains spatially coherent over much larger scales, leading to the presence of refractive substructure [?].

A recent observation of Sgr A<sup>\*</sup> at 3.5 mm by the VLBA+LMT [see Fig. reffig:substructure2 ?] has measured non-zero closure phases on its longest baselines. However it was also shown in the data analysis that the measured values are consistent with expectation refractive scintillation assuming a circular Gaussian source of FWHM = 130  $\mu$ -arcsec. Another observation at 1.3 cm shows flux modulation due to scattering substructure  $\sim 10$  mJy [?] and other predictions for  $\lambda = 1.3$  mm show  $\sim 60$  mJy for long East-West baselines and  $\sim 25$  mJy for long North-South baselines [?], assuming a Gaussian source of FWHM = 40  $\mu$ -arcsec.

Distinguishing intrinsic source and ISM substructure and variability is an interesting challenge. Observations at mm-wavelengths have revealed deviations from the  $\lambda^2$  scattering scaling law, see Fig. ???. This is interpreted as due to the presence of intrinsic source structure and has been fitted with a power-law with an exponent of  $1.34 \pm 0.01$  ?. This has enabled the constraint of various theoretical models ?, excluding advection-dominated accretion flows (ADAF) ? and Bondi-Hoyle accretion ?. However observations extending over month timescales are required to properly sample the larger scale inhomogeneities and even with multiple epoch observations, it can be difficult to distinguish source and scattering characteristics [?]. The developments in scattering theory presented above provide a robust mechanism for quantifying refractive effects. This could allow a decoupling without sampling a refractive ensemble but significant assumptions are always made on the source model.

### 1.2.3 Troposphere

The coherence and intensity of millimetre wavelength electromagnetic waves are most severely deteriorated in the lowest atmospheric layer, the troposphere which extends up to an altitude of 7 – 10 km above sea level and down to a temperature  $T \sim 218$  K [?]. The troposphere is composed of a number of different components including primary gases  $N_2$  and  $O_2$ , trace gases e.g. water vapour and  $CO_2$ , as well as particulates of water droplets and dust. The rest of this section will explore the tropospheric corruption for the mm-VLBI case beginning with insights from the fundamentals of electromagnetic propagation, followed by a review of atmospheric corruptions in the sub-mm regime. We then firm up our theory with a discussion on atmospheric radiative transfer and atmospheric turbulence.

### Propagation fundamentals

Consider a quasi-monochromatic wave passing through a linear medium,

$$E_\nu(x, t) = E_0 \exp^{i(kn_\nu x - 2\pi\nu t)}, \quad (1.24)$$

where  $k = 2\pi\nu/c$  is the propagation constant in free space and  $n = n_R + jn_I$  is the complex index of refraction. Note that we will occasionally omit the frequency dependence of  $n$  and related quantities to simplify the notation. If  $n_I$  is nonzero, the electric flux  $I$  will decay exponentially

$$I = EE^* = E_0^2 \exp(-\tau), \quad (1.25)$$

where  $\tau$  is called the opacity or optical depth and is related to the absorption coefficient,  $d\tau = \kappa dx$  where  $\kappa = 4\pi\nu n_I/c$ . If  $n_R > 1$  the phase velocity of light will decrease,  $v_p = c/n_R$ , which results in a time delay. The time delay due to the troposphere,  $\tilde{t}$  and opacity  $\tau$  can be calculated simultaneously,

$$\tilde{t} + i\tau/4\pi\nu = 1/c \int_{path} d\mathbf{s} (n_\nu(\mathbf{s}) - 1). \quad (1.26)$$

In the interferometric context opacity and time delay are often viewed independently. However, the electric field is real and causal which imposes restrictions on the complex refractive index. Specifically  $n_R$  and  $n_I$  contain the same information and can be interchanged via the Kramers-Kronig relations.

Absorption is accompanied by emission and for a medium in local thermodynamic equilibrium, Kirchoff's law states that

$$\frac{\epsilon_\nu}{\kappa_\nu} = B_\nu(T), \quad (1.27)$$

where  $\epsilon_\nu = dI_\nu/dx$  is the emission coefficient and  $B_\nu(T)$  is the Planck function. Hence the absorbing molecules are also emitters, increasing system

noise. Therefore opacity, time delay and atmospheric noise are interrelated and should be simulated consistently. On a side note these relations allow for phase calibration using measurements of sky emission via Water Vapour Radiometry (WVR) [e.g. ?].

### Atmospheric corruptions in the (sub-)mm regime

An analysis of the absorption spectrum in the GHz range (Fig. ??), shows that it is dominated by transitions of  $\text{H}_2\text{O}$  and  $\text{O}_2$  as well as a pseudo-continuum opacity which increases with frequency. The pseudo-continuum opacity is due to the cumulative effect of the far wings of a multitude of broadened water vapour lines above 1 THz [?]. At 230 GHz the absorption is typically 5 – 10% at the best sites, during good weather.

In contrast to the dry atmospheric components, water vapour mixes poorly and its time-variable spatial distribution induces rapid fluctuations in the time delays  $\tilde{t}$  above each station. The phase error for a baseline (1,2) where antenna 1 is the reference will be

$$\delta\phi(t, \nu) = 2\pi/\nu(\tilde{t}_2(t, \nu) - \tilde{t}_1(t, \nu)). \quad (1.28)$$

The water vapour column volume is measured as the depth of the column when converted to the liquid phase and is referred to as the precipitable water vapour (PWV). PWV is directly proportional to the time delay and hence the phase delay,

$$\delta\phi \approx \frac{12.6\pi}{\lambda} \times w, \quad (1.29)$$

where  $w$  is the depth of the PWV column [?] and an atmospheric temperature  $T = 270$  K has been assumed. This relationship between phase and water vapour content has been experimentally verified [?]. At 230 GHz, the change in PWV needed to offset the phase by 1 rad is  $\Delta w \approx 0.03$  mm.

This sensitive dependence of phase coherence on atmospheric stability

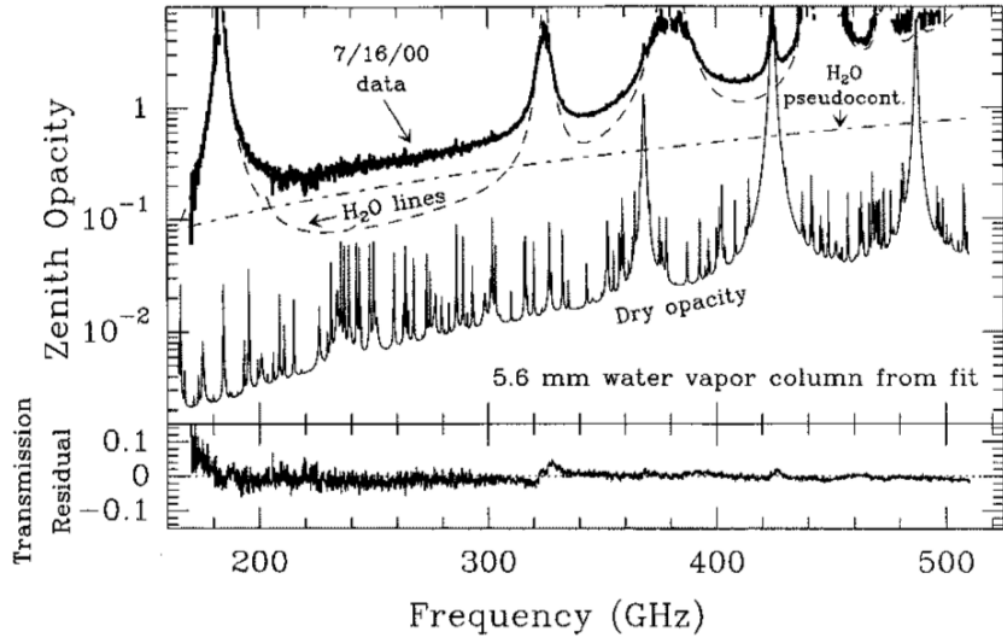


Figure 1.4: Recorded zenith absorption spectrum in the 160–520 GHz range, taken on Mauna Kea at an altitude of  $\approx 4000$  m. The data has been fit to a sum of H<sub>2</sub>O lines, an H<sub>2</sub>O pseudo-continuum and dry absorption lines. The model has been generated using the ATM code (see section ??), with the bottom panel showing the residuals. Here ‘dry’ refers to all atmospheric constituents except H<sub>2</sub>O. Reproduced from ?

is aggravated by three factors. First antenna elevation angles are typically fairly low for EHT observations which increases the atmospheric path length. Second as stations are far apart the atmospheric variations are uncorrelated between stations, this increases visibility decoherence as atmospheric variations appearing in both terms of equation ?? fall away. Third, observing with a sparse VLBI array means that there is less redundancy for calibration and so it is more difficult to separate source from atmospheric variations.

### Radiative transfer

The problem of radiative transfer through a static atmosphere is well described and implemented by the Atmospheric Transmission at Microwaves (ATM) software [?]. ATM has been incorporated into MEQSILHOUETTE to provide a fast and sophisticated procedure to calculate average opacities, sky brightness temperatures and time delays. Here we provide a brief summary of the theory underpinning the package but refer the reader to ? for more detail. ATM is commonly used in the Atacama Large Millimeter Array (ALMA) community [??] and has been tested with atmospheric transmission spectra taken on Mauna Kea [?].

We start from the unpolarised radiative transfer equation, which is unidirectional in the absence of scattering,

$$\frac{dI_\nu(s)}{ds} = \epsilon_\nu(s) - \kappa_\nu(s)I_\nu(s), \quad (1.30)$$

where  $s$  is the coordinate along the signal path through the atmosphere. We assume local thermodynamic equilibrium (LTE) which should hold as the collisional timescale is much smaller than the time for spontaneous emission for all but the highest part of the atmosphere. Applying equation ??, multiplying by  $\exp(-\tau_\nu)$  and integrating from the top of the atmosphere ( $s = 0$ ) yields,

$$I_\nu(s) = I_\nu(0)e^{-\tau_\nu(0,s)} + \int_0^s B_\nu(s')e^{-\tau_\nu(s',s)}\kappa_\nu(s')ds', \quad (1.31)$$

where  $s'$  is a dummy variable in the same direction as  $s$  and  $\tau_\nu(0, s) = \int_0^s k_\nu(s') ds'$ .  $I_\nu(0)$  is normally taken as the radiance from the cosmic background. To calculate the  $I_\nu(s)$ ,  $\tau(s)$  and complete the above integral, requires  $\kappa_\nu$  as a function of altitude and frequency. The time delay  $\tilde{t}$  can be calculated from  $\tau$  using the Kramers-Kronig relations.

A general equation to determine the absorption coefficient for a transition between a lower  $l$  and upper  $u$  states is given in the original paper. Here we merely point out that it should be proportional to the energy of the photon,  $h\nu_{l \rightarrow u}$ , the transition probability or Einstein coefficient,  $B_{l \rightarrow u}$ , the line-shape,  $f(\nu, \nu_{l \rightarrow u})$  and the number densities  $N$  of electronic populations. Line profiles which describe pressure broadening (perturbations to the Hamiltonian due to the presence of nearby molecules) and Doppler broadening are used. The condition of detailed balance further requires that decays from the upper state are included yielding,  $g_u B_{u \rightarrow l} = g_l B_{l \rightarrow u}$ , where  $g$  is the degeneracy of the electronic state. Putting this together we find,

$$\kappa(\nu)_{l \rightarrow u} \propto h\nu B_{l \rightarrow u} \left( \frac{N_l}{g_l} - \frac{N_u}{g_u} \right) f(\nu, \nu_{l \rightarrow u}), \quad (1.32)$$

where the Einstein coefficients are calculated from the inner product of the initial and final states with the dipole transition operator,

$$B_{l \rightarrow u} = \frac{2\pi}{3\hbar^2} | \langle u | \mu | l \rangle |^2, \quad (1.33)$$

where  $|u\rangle$ ,  $|l\rangle$ ,  $|\mu\rangle$  are the wavefunctions of upper and lower states and the dipole transition operator respectively. The number densities of the two states,  $N_u$  and  $N_l$  in local thermodynamic equilibrium (LTE) are simply related to the local number density and temperature via Boltzmann statistics.

$$\frac{N_n}{N} = g_n \frac{\exp -\frac{E_n}{kT}}{Q} \quad (1.34)$$

where  $Q$  is the partition function.  $Q = \sum_i g_i \exp -E_i/kT$ . Transition lines



at radio wavelengths result from rotational state transitions. To calculate the inner product given in equation ??, Operators which describe linearly symmetric rotors (e.g. O<sub>2</sub>, CO) and asymmetric rotors are used. The asymmetric rotations are decomposed into three principal rotation axes with differing rotational constants governing each axis. Rotational constants were measured by the authors as well as drawn from a variety of literature. Partition functions and transition probability are calculated using approximations taken from the literature.

Far wing broadening of H<sub>2</sub>O lines > 1.2 THz extends to lower frequencies and is not completely represented by the line-shape used. This is believed to be due to self-self collisions of water molecules. Additionally there are terms from the dry atmosphere related to transient dipoles and Debye absorption which are not represented in the line-shape. To correct for these effects, two pseudocontinua are used. These are modelled as a power law dependence on frequency, temperature and the molecular densities.

### **Turbulent phase fluctuations**

Visibility phase instability  $\delta\phi(t)$  due to tropospheric turbulence is a fundamental limitation to producing high fidelity, science-quality maps with a mm-VLBI array [?]. The coherence time-scale is typically too rapid ( $\lesssim 10$  s) for fast switching calibration, so other calibration procedures (e.g. water vapour radiometry, paired antennas, and/or self-calibration) must be performed. Self-calibration is the most commonly used but is limited by the integration time needed to obtain adequate SNR to fringe fit. Phase decoherence often leads to the use of closure quantities to perform model fitting [???], and causes a decrease in measured flux due to incoherent complex averaging. In the section we will review and develop the weak scattering theory introduced earlier which will culminate in a formulation for the simulation of tropospheric phase turbulence seen by a mm-VLBI array. How this formulation is implemented and fits into the broader atmospheric simulation

framework will be discussed in section ??.

Following from section ??, we model the statistics of  $\delta\phi(t)$  with a thin, frozen, Kolomogorov-turbulent phase screen moving with a bulk velocity,  $v$ . However, the turbulent layer has a definite width  $\Delta h$  and both Kolmorogov theory and measurement [Fig. ??, ???] show that this brings in a new regime

$$\beta = \begin{cases} 5/3 & \text{if } r < \Delta h, \\ 2/3 & \text{if } r > \Delta h, \\ 0 & \text{if } r > r_{\text{out}}. \end{cases} \quad (1.35)$$

In Fig. ?? we can see estimations of  $\Delta h \approx 1$  km and  $r_{\text{out}} \approx 6$  km. We will show later that even though we are working with a VLBI array, our implementation falls in into the  $r \ll \Delta h$  regime.

We set the height  $h$  of the screen at the water vapour scale height of 2 km above ground. At 1.3 mm, the Fresnel scale is  $r_F \approx 0.45$  m and experiments show annual variations of  $r_0 \sim 50 - 500$  m above Mauna Kea [?] and  $r_0 \sim 90 - 700$  m above Chajnantor [?], where both sites are considered to have excellent atmospheric conditions for millimetre astronomy. As  $r_F < r_0$ , this is an example of weak scattering.

The required field-of-view (FoV) of a global mm-VLBI array is typically  $\text{FoV} < 1$  mas or  $\sim 10 \mu\text{m}$  at a height of 2 km, which is roughly 7-8 orders of magnitude smaller than the tropospheric coherence length. The tropospheric corruption can therefore be considered constant across the FoV and, from the perspective of the Measurement Equation, modeled as a diagonal Jones matrix per time and frequency interval. As VLBI baselines are much longer than the coherence length,  $|\mathbf{b}| \geq 1000 \text{ km} \gg r_0$ , the phase screen at each site must be simulated independently. This assumption only holds for VLBI baselines and the framework needs to be extended to simulate the effects of turbulence on individual phased arrays stations (e.g. SMA) and short ( $< 10$  km) baselines (e.g. JCMT - SMA).

Our aim then is to produce a phase error time sequence  $\{\delta\phi(t_i)\}$  for

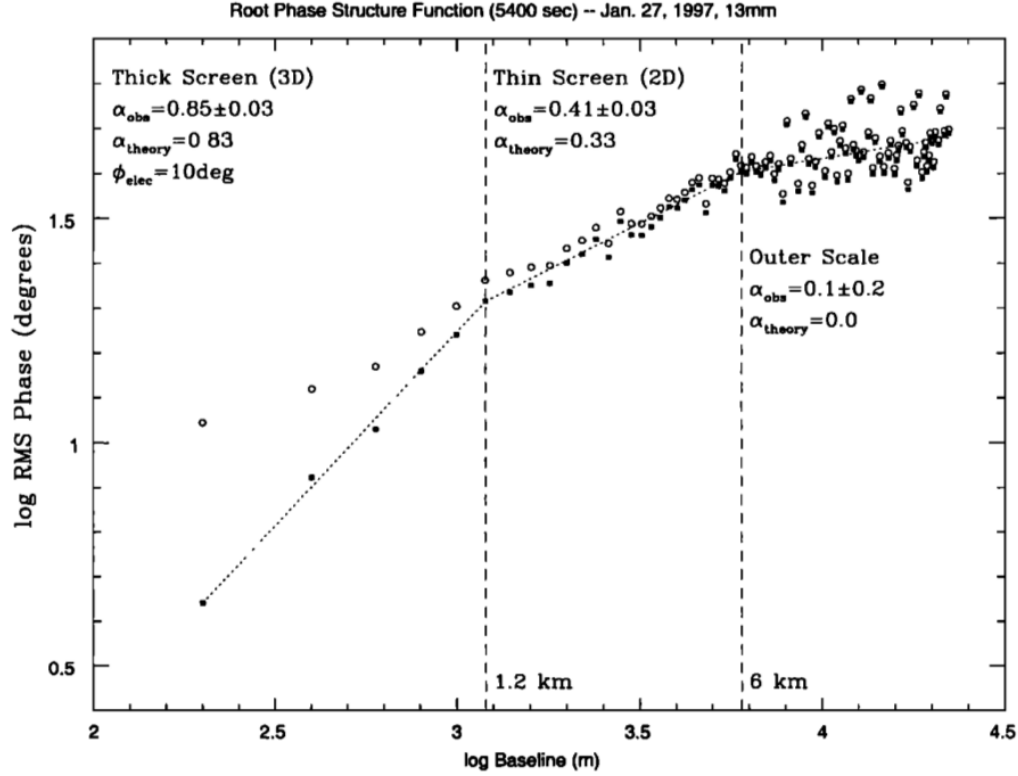


Figure 1.5: A log-log plot of RMS visibility phase versus baseline length for an observation of 1 Jy source 0748 + 240 with VLA at 22 GHz over a 90 min duration. The open circles show RMS phase as measured whereas the solid squares show the same values with a constant thermal noise contribution of  $10^\circ$  subtracted in quadrature. Note that the measured and theoretical Kolmogorov turbulent exponent  $\beta$  changes with distance on the phase screen as the viewing configuration transitions from a thick screen ( $\beta_{\text{theory}} = 5/3$ ) to a thin screen ( $\beta_{\text{theory}} = 2/3$ ) at  $r \approx 1$  km and from a thin screen to completely uncorrelated regime ( $\beta = 0$ ) beyond the outer scale at  $r \approx 6$  km. Although these regimes appear distinct, there is continuous variation between them. Reproduced from ?

each station which is added to the visibility phase. We invoke the frozen screen assumption and write the structure function as a function of time,  $D(t) = D(r)|_{r=vt}$ . The temporal structure function  $D(t)$  provides an efficient route to sample the variability of the troposphere at the typical integration time of the dataset,  $t_{\text{int}} \sim 1$  sec.

The temporal variance of the phase is a function of the temporal structure function, and accounting for time integration yields [see ?, B3]

$$\sigma_\phi^2(t_{\text{int}}) = (1/t_{\text{int}})^2 \int_0^{t_{\text{int}}} (t_{\text{int}} - t) D_\phi(t) dt. \quad (1.36)$$

Assuming power-law turbulence and integrating yields,

$$\sigma_\phi^2(t_{\text{int}}) = \left[ \frac{1}{\sin \theta (\beta^2 + 3\beta + 2)} \right] \left( \frac{t_{\text{int}}}{t_0} \right)^\beta, \quad (1.37)$$

where  $t_0 = r_0/v$  is the coherence time when observing at zenith and  $1/\sin \theta$  is the approximate airmass which arises as  $D_\phi \propto w$ . As  $r \ll \Delta h$ , where  $\Delta h$  is the thickness of the turbulent layer, an thin screen exponent of  $\beta = 5/3$  is justified [?]. The phase error time-series takes the form of a Gaussian random walk per antenna. At mm-wavelengths, the spectrum of water vapour is non-dispersive up to a few percent [?] and so we can assume a simple linear scaling across the bandwidth.

Phase fluctuations  $\delta\phi(t)$  can also be simulated by taking the inverse Fourier transform of the spatial phase power spectrum. However this approach is much more computationally expensive, e.g. for an observation length  $t_{\text{obs}}$  involving  $N_{\text{ant}} = 8$  independent antennae with dish radii  $r_{\text{dish}} = 15$  m, wind speed  $v = 10 \text{ m s}^{-1}$  and pixel size equal to  $r_{\text{F}}$ , the number of pixels  $N_{\text{pix}} \approx N_{\text{ant}} t_{\text{obs}} r_{\text{dish}}^2 / (v r_{\text{F}}^3) \sim 10^8$ . Additionally, due to fractal nature of ideal Kolmogorov turbulence, the power spectrum becomes unbounded as the wavenumber approaches zero which makes it difficult to determine the sampling interval of the spatial power spectrum [?].

### 1.2.4 Instrumental

All instruments suffer from both systematic and stochastic errors, the characterisation of which are essential to high precision measurement. In this section we explore thermal noise (stochastic) and antenna pointing errors (systematic). While there are many additional potential sources of error (e.g. clock errors, bandpass, polarisation leakage, phasing errors, quantisation, correlator model, etc.). The point here is to demonstrate the mm-VLBI framework that enables more sophisticated interferometric simulations. The Measurement Equation formalism, enables any arbitrary linear error to be incorporated as a Jones Matrix e.g. a bandpass error would be a frequency-dependent diagonal Jones matrix.

#### Thermal Noise

The level of thermal noise of measurement defines the absolute limit on the sensitivity of the interferometer to detect a source and also to distinguish fine source characteristics. Closure quantities are especially prone to high levels of thermal as several visibilities are multiplied. A derivation of the thermal noise of an interferometer can be made through derivation of the thermal noise of an antenna and then correlating the result [?]. The RMS thermal noise of an interferometer  $\{i, j\}$  over a bandwidth  $\Delta\nu$  and an integration time is given by

$$\Delta S_{ij} = \frac{1}{\eta_s} \sqrt{\frac{SEFD_i SEFD_j}{2\Delta\nu t_{\text{int}}}}, \quad (1.38)$$

where  $\eta_s$  is the system efficiency and  $2\Delta\nu t_{\text{int}}$  is the number of independent samples. The  $SEFD$  is a measure of the sensitivity of an antenna, accounting for the efficiency, collecting area and thermal noise and is defined as the flux density of a source with the same power,

$$SEFD = 2k_B T_{\text{sys}} / (\eta_a A), \quad (1.39)$$

where  $A$  is the antenna area,  $\eta_a$  is the antenna efficiency,  $T_{\text{sys}}$  is the system temperature and the factor  $\frac{1}{2}$  accounts for only sampling 1 polarisation.

As the RIME was formulated for a thermal noise-free measurement, we do not apply this corruption as a multiplicative matrix but rather an additive matrix,

$$\mathbf{V}_{pq} = \mathbf{G}_p \mathbf{X}_{pq} \mathbf{G}_q^H + \mathbf{N}_{pq}, \quad (1.40)$$

where each component of  $\mathbf{N}_{pq} \sim (0, \Delta S_{ij}^2)$ .

### Antenna Pointing

All antennas suffer pointing errors to some degree due to a variety of factors including dish flexure due to gravity, wind and thermal loading, as well as drive mechanics. This corresponds to an offset primary beam, which should only translate to minor amplitude errors if the pointing error  $\theta_{\text{PE}}$  is significantly smaller than the primary beam (i.e.  $\theta_{\text{PE}} \ll \theta_{\text{PB}}$ ). In the Measurement Equation formalism, this offset can be represented by a modified (shifted) primary beam pattern in the  $E$ -Jones term

$$\mathbf{E}_p(l, m) = \mathbf{E}(l_0 + \delta l_p, m_0 + \delta m_p), \quad (1.41)$$

where  $\delta l_p, \delta m_p$  correspond to the directional cosine offsets. This could be a problem for millimetre observations as the primary beam is significant, e.g. for a 30 m dish at 1.3 mm,  $\theta_{\text{PB}} \sim 10$  arcsec, compared to the  $\theta_{\text{PE}} \sim 1$  arcsec.

We identify two main classes of pointing error. Firstly an antenna tracking a source will suffer a slow, continuous time-variable pointing error associated with the tracking error  $\sigma_{\text{track}}$ . Physically this could be attributed to changes in wind, thermal and gravitational loading which all change with telescope pointing direction and over the course of a typical few hour observation. Using the MeqTrees software package, such behaviour has been demonstrated to occur with the Westerbork Synthesis Radio Telescope (WSRT, Smirnov

[2011c])<sup>1</sup>.

Secondly, whilst a stationary phase centre is tracked, the pointing error should evolve slowly and smoothly, however, in mm-VLBI observations the phase centre is often shifted to another source/calibrator. This would cause the pointing error to change abruptly, with an absolute pointing error  $\sim \sigma_{\text{abs}}$ . Source/calibrator change is scheduled every 5-10 minutes in a typical millimetre observation. The point is that even though EHT will be able to determine the pointing offset when observing a calibrator with well known structure, when the antennas slew back to a source (e.g. Sgr A<sup>\*</sup>) with less certain or variable source structure, the pointing error could change significantly. This is exacerbated by the scarcity of mm-wavelength calibrators, which are often widely separated from the source.

---

<sup>1</sup>See also <https://indico.skatelescope.org/event/171/session/9/contribution/20>

# Bibliography

- T. Blecher, R. Deane, G. Bernardi, and O. Smirnov. MeqSilhouette : A mm-VLBI observation and signal corruption simulator. *ArXiv e-prints*, August 2016.
- K. L. Bouman, M. D. Johnson, D. Zoran, V. L. Fish, S. S. Doeleman, and W. T. Freeman. Computational Imaging for VLBI Image Reconstruction. *ArXiv e-prints*, dec 2015.
- A. E. Broderick, V. L. Fish, S. S. Doeleman, and A. Loeb. Constraining the Structure of Sagittarius A\*’s Accretion Flow with Millimeter Very Long Baseline Interferometry Closure Phases. *ApJ*, 738:38, September 2011. doi: 10.1088/0004-637X/738/1/38.
- Avery E. Broderick and Abraham Loeb. IMAGING THE BLACK HOLE SILHOUETTE OF M87: IMPLICATIONS FOR JET FORMATION AND BLACK HOLE SPIN. *ApJ*, 697(2):1164–1179, may 2009. doi: 10.1088/0004-637x/697/2/1164. URL <http://dx.doi.org/10.1088/0004-637x/697/2/1164>.
- Avery E. Broderick, Tim Johannsen, Abraham Loeb, and Dimitrios Psaltis. TESTING THE NO-HAIR THEOREM WITH EVENT HORIZON TELESCOPE OBSERVATIONS OF SAGITTARIUS A\*. *ApJ*, 784(1):7, feb 2014. doi: 10.1088/0004-637x/784/1/7. URL <http://dx.doi.org/10.1088/0004-637x/784/1/7>.



- Avery E. Broderick, Vincent L. Fish, Michael D. Johnson, Katherine Rosenfeld, Carlos Wang, Sheperd S. Doeleman, Kazunori Akiyama, Tim Johannsen, and Alan L. Roy. MODELING SEVEN YEARS OF EVENT HORIZON TELESCOPE OBSERVATIONS WITH RADIATIVELY INEFFICIENT ACCRETION FLOW MODELS. *ApJ*, 820(2):137, mar 2016. doi: 10.3847/0004-637x/820/2/137. URL <http://dx.doi.org/10.3847/0004-637x/820/2/137>.
- A. A. Chael, M. D. Johnson, R. Narayan, S. S. Doeleman, J. F. C. Wardle, and K. L. Bouman. High Resolution Linear Polarimetric Imaging for the Event Horizon Telescope. *ArXiv e-prints*, May 2016.
- S. Doeleman, E. Agol, D. Backer, F. Baganoff, G. C. Bower, A. Broderick, A. Fabian, V. Fish, C. Gammie, P. Ho, M. Honman, T. Krichbaum, A. Loeb, D. Marrone, M. Reid, A. Rogers, I. Shapiro, P. Strittmatter, R. Tilanus, J. Weintroub, A. Whitney, M. Wright, and L. Ziurys. Imaging an Event Horizon: submm-VLBI of a Super Massive Black Hole. In *astro2010: The Astronomy and Astrophysics Decadal Survey*, volume 2010 of *Astronomy*, 2010.
- Sheperd S. Doeleman, Jonathan Weintroub, Alan E. E. Rogers, Richard Plambeck, Robert Freund, Remo P. J. Tilanus, Per Friberg, Lucy M. Ziurys, James M. Moran, Brian Corey, Ken H. Young, Daniel L. Smythe, Michael Titus, Daniel P. Marrone, Roger J. Cappallo, Douglas C.-J. Bock, Geoffrey C. Bower, Richard Chamberlin, Gary R. Davis, Thomas P. Krichbaum, James Lamb, Holly Maness, Arthur E. Niell, Alan Roy, Peter Strittmatter, Daniel Werthimer, Alan R. Whitney, and David Woody. Event-horizon-scale structure in the supermassive black hole candidate at the Galactic Centre. *Nature*, 455(7209):78–80, sep 2008. doi: 10.1038/nature07245. URL <http://dx.doi.org/10.1038/nature07245>.
- Sheperd S. Doeleman, Vincent L. Fish, Avery E. Broderick, Abraham Loeb, and Alan E. E. Rogers. DETECTING FLARING STRUCTURES IN

- SAGITTARIUS A\* WITH HIGH-FREQUENCY VLBI. *ApJ*, 695(1):59–74, mar 2009. doi: 10.1088/0004-637x/695/1/59. URL <http://dx.doi.org/10.1088/0004-637x/695/1/59>.
- H Falcke and S B Markoff. Toward the event horizon—the supermassive black hole in the Galactic Center. *Class. Quantum Grav.*, 30(24):244003, nov 2013. doi: 10.1088/0264-9381/30/24/244003. URL <http://dx.doi.org/10.1088/0264-9381/30/24/244003>.
- Heino Falcke, W. M. Goss, Hiroshi Matsuo, Peter Teuben, Jun-Hui Zhao, and Robert Zylka. The Simultaneous Spectrum of Sagittarius A\* from 20 Centimeters to 1 Millimeter and the Nature of the Millimeter Excess. *ApJ*, 499(2):731–734, jun 1998. doi: 10.1086/305687. URL <http://dx.doi.org/10.1086/305687>.
- Vincent L. Fish, Michael D. Johnson, Ru-Sen Lu, Sheperd S. Doeleman, Katherine L. Bouman, Daniel Zoran, William T. Freeman, Dimitrios Psaltis, Ramesh Narayan, Victor Pankratius, Avery E. Broderick, Carl R. Gwinn, and Laura E. Vertatschitsch. IMAGING AN EVENT HORIZON: MITIGATION OF SCATTERING TOWARD SAGITTARIUS A\*. *ApJ*, 795(2):134, oct 2014. doi: 10.1088/0004-637x/795/2/134. URL <http://dx.doi.org/10.1088/0004-637x/795/2/134>.
- S. Gillessen, F. Eisenhauer, T. K. Fritz, H. Bartko, K. Dodds-Eden, O. Pfuhl, T. Ott, and R. Genzel. The Orbit of the Star S2 Around SGR A\* from Very Large Telescope and Keck Data. *ApJ*, 707:L114–L117, December 2009. doi: 10.1088/0004-637X/707/2/L114.
- C. Goddi, H. Falcke, M. Kramer, L. Rezzolla, C. Brinkerink, T. Bronzwaer, R. Deane, M. De Laurentis, G. Desvignes, J. R. J. Davelaar, F. Eisenhauer, R. Eatough, R. Fraga-Encinas, C. M. Fromm, S. Gillessen, A. Grenzebach, S. Issaoun, M. Janßen, R. Konoplya, T. P. Krichbaum, R. Laing, K. Liu, R.-S. Lu, Y. Mizuno, M. Moscibrodzka, C. Müller, H. Olivares, O. Porth,

- O. Pfuhl, E. Ros, F. Roelofs, K. Schuster, R. Tilanus, P. Torne, I. van Bemmelen, H. J. van Langevelde, N. Wex, Z. Younsi, and A. Zhidenko. BlackHoleCam: fundamental physics of the Galactic center. *ArXiv e-prints*, June 2016.
- J. P. Hamaker, J. D. Bregman, and R. J. Sault. Understanding radio polarimetry. I. Mathematical foundations. *A&AS*, 117:137–147, May 1996.
- T. Johannsen and D. Psaltis. Testing the No-hair Theorem with Observations in the Electromagnetic Spectrum. II. Black Hole Images. *ApJ*, 718:446–454, July 2010. doi: 10.1088/0004-637X/718/1/446.
- T. P. Krichbaum, D. A. Graham, A. Witzel, A. Greve, J. E. Wink, M. Grewing, F. Colomer, P. de Vicente, J. Gomez-Gonzalez, A. Baudry, and J. A. Zensus. VLBI observations of the galactic center source SGR A\* at 86 GHz and 215 GHz. *A&A*, 335:L106–L110, July 1998.
- R.-S. Lu, F. Roelofs, V. L. Fish, H. Shiokawa, S. S. Doeleman, C. F. Gammie, H. Falcke, T. P. Krichbaum, and J. A. Zensus. Imaging an Event Horizon: Mitigation of Source Variability of Sagittarius A\*. *ApJ*, 817:173, February 2016. doi: 10.3847/0004-637X/817/2/173.
- Ru-Sen Lu, Avery E. Broderick, Fabien Baron, John D. Monnier, Vincent L. Fish, Sheperd S. Doeleman, and Victor Pankratius. IMAGING THE SUPERMASSIVE BLACK HOLE SHADOW AND JET BASE OF M87 WITH THE EVENT HORIZON TELESCOPE. *ApJ*, 788(2):120, may 2014. doi: 10.1088/0004-637x/788/2/120. URL <http://dx.doi.org/10.1088/0004-637x/788/2/120>.
- M. Mościbrodzka, H. Falcke, H. Shiokawa, and C. F. Gammie. Observational appearance of inefficient accretion flows and jets in 3D GRMHD simulations: Application to Sagittarius A\*. *A&A*, 570:A7, October 2014. doi: 10.1051/0004-6361/201424358.

- J. E. Noordam and O. M. Smirnov. The MeqTrees software system and its use for third-generation calibration of radio interferometers. *A&A*, 524:A61, nov 2010. doi: 10.1051/0004-6361/201015013. URL <http://dx.doi.org/10.1051/0004-6361/201015013>.
- Dimitrios Psaltis, Norbert Wex, and Michael Kramer. A QUANTITATIVE TEST OF THE NO-HAIR THEOREM WITH Sgr A\* USING STARS PULSARS AND THE EVENT HORIZON TELESCOPE. *ApJ*, 818(2):121, feb 2016. doi: 10.3847/0004-637x/818/2/121. URL <http://dx.doi.org/10.3847/0004-637x/818/2/121>.
- E. Serabyn, J. Carlstrom, O. Lay, D. C. Lis, T. R. Hunter, J. H. Lacy, and R. E. Hills. High-Frequency Measurements of the Spectrum of Sagittarius A\*. *ApJ*, 490(1):L77–L81, nov 1997. doi: 10.1086/311010. URL <http://dx.doi.org/10.1086/311010>.
- O. M. Smirnov. Revisiting the radio interferometer measurement equation. *A&A*, 527:A106, 2011a. doi: 10.1051/0004-6361/201016082. URL <http://dx.doi.org/10.1051/0004-6361/201016082>.
- O. M. Smirnov. Revisiting the radio interferometer measurement equation. *A&A*, 527:A107, 2011b. doi: 10.1051/0004-6361/201116434. URL <http://dx.doi.org/10.1051/0004-6361/201116434>.
- O. M. Smirnov. Revisiting the radio interferometer measurement equation. *A&A*, 527:A108, 2011c. doi: 10.1051/0004-6361/201116435. URL <http://dx.doi.org/10.1051/0004-6361/201116435>.
- R. Takahashi. Shapes and Positions of Black Hole Shadows in Accretion Disks and Spin Parameters of Black Holes. *ApJ*, 611:996–1004, August 2004. doi: 10.1086/422403.